# Robust Initial Orbit Determination Using Streaks and Admissible Regions

**Sam Wishnek**
*The University of Colorado at Boulder, Smead Aerospace Engineering Sciences Department*
**Marcus Holzinger**
*The University of Colorado at Boulder, Smead Aerospace Engineering Sciences Department*

**Patrick Handley**
*Ball Aerospace*

## ABSTRACT

A novel, empirically-validated method for robust initial orbit determination from two or more observations of an object's angles and angle rates is presented. The method can be applied for all orbital regimes including those where traditional methods, such as Gauss, double-r, and Laplace fail. It also works for all times-of-flight to produce the corresponding set of feasible orbit solutions using admissible regions.

The method uses a proposed cost function that has a unique non-trivial zero at the correct orbit solution for the single revolution case and a set of zeros for the multi-orbit case. Because the system is overdetermined with the minimum two measurements, the global minimum will not approach zero if the two observations do not correspond to the same orbiting object. Applying a particle swarm descent or Nelder-Mead method to the problem allows the system to converge to the correct state for any orbital regime. In its most natural implementation this problem is a four-dimensional search. However, by projecting one measurement into the space of the other, it can be solved with a pair of two-dimensional searches which is much more computationally efficient and parallelizable. Applying admissible regions to both observations allows the state space to be further constrained with a corresponding improvement to the computational efficiency. In addition, the particle swarm and Nedler-Mead approaches can report all of the feasible states in the multi-revolution case. The proposed method overcomes the shortcomings of many traditional initial orbit determination methods and has been empirically verified to find solutions to cases well-approximated by two-body dynamics.

Furthermore, this work includes a comparison of the proposed and existing methods for initial orbit determination to highlight the domains that the various methods excel. While the global optimizer approach of the proposed method sacrifices computation time in comparison to the single iteration of the previously established methods, it consistently converges to the correct solution or set of possible solutions independent of the orbital regime.

## 1. INTRODUCTION

Observations of space objects, both natural and artificial come in two main forms. These are radio observations that can accurately measure range and range rate of a target object with more approximate angular information and optical measurements that can accurately report a heading vector pointing from the observer to the target. Depending on the type of observation and the number of observations of a target object, there are a plethora of options for how to process these observations in order to estimate the true state of a target object. When the data set consists of many observations, non-linear batch or Kalman filters can be useful tools for finding an accurate estimated state [15]. However, when the data set is more limited, there are a number of initial orbit determination (IOD) methods available that can be applied to find an estimated state.

There are a variety of initial orbit determination methods available. In terms of methods available for state estimation from optical data, there are two main types of algorithms. There are methods that accept only relative angle measurements between the observer and the target, and there are methods that accept the first time derivative of the heading as

Copyright © 2020 Advanced Maui Optical and Space Surveillance Technologies Conference (AMOS) – www.amostech.com

well. These are angles-only methods and angle and angle rates methods respectively [17]. In addition, many of these methods are more likely to converge in specific scenarios. Methods such as Laplace and Gauss tend to struggle with targets in low-Earth orbit as these methods perform best when the angle between observations is small. This narrows the feasible time windows between observations that allow these methods to remain useful [8]. Other angles-only methods like P.R. Escobal's double-r method work well with large angles between measurements. However, the iterative double-r algorithm has a relatively tight constraint on the initial guess for the target ranges that allows the method to converge to the correct solution [5]. The popular Gooding method often fails for space-based observers [8][6].

The variety in effective and ineffective regimes for these different approaches poses problems in itself. When little is known about a target object, it is not always clear which methods should be applied in order to find an accurate estimate of the true state. In addition, there are cases that do not perform particularly well under any initial orbit determination approach. One major case of this is for space-based observers measuring targets with large angles of separation between observations and little to no a-priori knowledge for generating initial guesses for the observation ranges.

Most of the previously mentioned IOD algorithms are angles-only methods. These algorithms require a minimum of three observations to generate a state estimate as each measurement only provides two constraints while the system has six degrees of freedom. There are cases where a single optical observation of a space object can provide two additional constraints in the form of angle rate measurements. If the optical system translational and rotational rates of motion are known, the angle rates can be extracted from a single image. In this case, a minimum of two observations are required to estimate a full six degree of freedom state [15].

One promising approach for orbit determination is the $L_n$ and similar $J_n$ approaches developed by Rema Raymond Karimi and Daniele Mortari [7]. They showed in their 2011 paper how these angles-only algorithms could perform well in a variety of scenarios with only the zero vector as the initial range estimate.

The proposed method starts as an adaption of $L_n$ rederived to accept angle rates and angles instead of only angles [7]. The $L_n$ method uses a least squares optimization to find a solution that satisfies an equality based on the universal variable formulation of two body dynamics. The solution space contours of a cost function based on this approach show that the solution space has several local minima that can divert the algorithm from the correct solution for geometries where the target orbit lies inside the observer orbit. This cost function can then be searched with a global optimizing algorithm to find the solution corresponding to the true state.

The new proposed cost function has a unique non-trivial zero at the correct orbit solution. Because the system is overdetermined with the minimum two measurements, the global minimum will not approach zero if the two observations do not correspond to the same orbiting object. Applying a particle swarm descent method to the problem allows the system to converge to the correct state for any orbital regime. In its most natural implementation this problem is a four-dimensional search. However, by projecting one measurement into the space of the other, it can be solved with a pair of two-dimensional searches which is much more computationally efficient and parallelizable. Applying admissible regions to both observations allows the state space to be further constrained with a corresponding improvement to the computational efficiency. In addition, the particle swarm approach can report all of the feasible states in the multi-revolution case. The proposed method overcomes the shortcomings of many traditional initial orbit determination methods and has been empirically verified to find solutions to cases well-approximated by two-body dynamics. In addition, a Nelder-Mead optimization applied over the same cost function can show how the different optimization methods can impact computation time.

## 2. THEORY

### 2.1 Initial Orbit Determination with Lagrangian Coefficients

Much of the work covered in this paper is inspired by extending the work of Reza Raymond Karimi and Daniele Mortari in their 2010 paper [7]. Their approach to angles only initial orbit determination started with the Lagrange coefficients from the universal variable formulation of the two-body Kepler's problem. The approach applied the Lagrange coefficients to express the position state of the target spacecraft as a linear combination of the position state vectors at the previous and subsequent times. The position states then are broken down into their angular and range components. The full system can be expressed as a linear equation by pulling the ranges out as the independent vector. This is shown in equation 1. The $c_i$ and $d_i$ terms represent the coefficients used to express the $i^{th}$ position vector in

Copyright © 2020 Advanced Maui Optical and Space Surveillance Technologies Conference (AMOS) – www.amostech.com

terms of its previous and subsequent position states respectively. The $\hat{\rho}_i$ vectors are the unit vector headings from the observer position to the target position. The $\rho_i$ terms are the ranges. Finally, $\vec{\xi}_i = \vec{R}_i - c_i\vec{R}_{i-1} - d_i\vec{R}_{i+1}$ where $R_i$ corresponds to the observer position at the $i^{th}$ measurement [7].

$$\begin{bmatrix} c_2\hat{\rho}_i & -\hat{\rho}_2 & d_2\hat{\rho}_3 & \vec{0} & \vec{0} & \dots & \vec{0} \\ \vec{0} & c_3\hat{\rho}_2 & -\hat{\rho}_3 & d_3\hat{\rho}_4 & \vec{0} & \dots & \vec{0} \\ \vec{0} & \vec{0} & c_3\hat{\rho}_3 & -\hat{\rho}_4 & d_4\hat{\rho}_5 & \dots & \vec{0} \\ \vdots & \vdots & \vdots & \vdots & \vdots & \ddots & \vdots \\ \vec{0} & \vec{0} & \vec{0} & \vec{0} & \vec{0} & \dots & d_{n-1}\hat{\rho}_n \end{bmatrix} \begin{bmatrix} \rho_1 \\ \rho_2 \\ \rho_3 \\ \vdots \\ \rho_n \end{bmatrix} = \begin{bmatrix} \vec{\xi}_2 \\ \vec{\xi}_2 \\ \vec{\xi}_3 \\ \vdots \\ \vec{\xi}_{n-1} \end{bmatrix} \tag{1}$$

### 2.2 Extension to Include Angle Rates

As the initial orbit determination method as presented by Karimi and Mortari accepts only relative angle of the target object as seen by the observer, the algorithm requires a minimum of three observations of the target object in order to provide an estimate of the target's orbit. The three observations each represent two degrees of freedom and the six total matches the full six degree-of-freedom translational state. However, some methods for observing space objects can readily yield angles and angle rates in a single measurement. For example, a non-tracking optical image taken with a relatively long integration time can show a streak instead of a point source for the target object's location. The direction and length of the streak can be used to estimate the target's angular rate with a single image. A measurement of both the target's angles and angle rates provides four degrees of freedom in a single measurement. In this case, only two measurements are required to establish an overdetermined estimate of the target's full six degree-of-freedom state. This both allows for a more efficient use of the collected data and reduced the minimum number of observations required to determine a state.

The angles-only method acts as a starting point for the derivation of a similar method that integrates angle rates as well. Both approaches start with two expressions for the position of the target object. One is defined with equation (2), while the other definition comes from equation (4). Instead of combining these equations for three different measurement times, two additional equations for velocity are added in with the two position equations. These are an equation for velocity based on heading, heading rate, range, and range rate values as shown in equation (3). The other is the Lagrange coefficient equation for velocity as shown in equation (5). Equations (2) and (3) can be substituted into equations (4) and (5) for every instance of a target position or state vector. This will yield equations (6) and (7) which are only in terms of three types of parameters. These are the known parameters, $\vec{R}$ and $\dot{\vec{R}}$, the measured parameters, $\vec{p}$ and $\dot{\vec{p}}$, the range and range rate and the Lagrange coefficients that depend on the other parameters.

The Lagrange coefficients come from the universal variable formulation of the two-body Kepler problem. The variables $f$, $g$, $\dot{f}$, and $\dot{g}$ are derived directly from the dynamics of the physical system, and the formulaic definitions of these four terms are provided in equations (10) through (13) [14]. These four values are defined in terms of the translational inertial state vectors $\vec{r}_1$, $\vec{r}_2$, $\dot{\vec{r}}_1$, and $\dot{\vec{r}}_2$. These can be found from the known observer state, measured heading to the target and rate, and estimated range and range rate with equations (2) and (3).

$$\vec{r}_k = \vec{R}_k + \rho_k\vec{p}_k \tag{2}$$

$$\dot{\vec{r}}_k = \dot{\vec{R}}_k + \dot{\rho}_k\vec{p}_k + \rho_k\dot{\vec{p}}_k \tag{3}$$

$$\vec{r}_{k+1} = f_k\vec{r}_k + g_k\dot{\vec{r}}_k \tag{4}$$

$$\dot{\vec{r}}_{k+1} = \dot{f}_k\vec{r}_k + \dot{g}_k\dot{\vec{r}}_k \tag{5}$$

$$\vec{R}_{k+1} + \rho_{k+1}\vec{p}_{k+1} = f_k\left(\vec{R}_k + \rho_k\vec{p}_k\right) + g_k\left(\dot{\vec{R}}_k + \dot{\rho}_k\vec{p}_k + \rho_k\dot{\vec{p}}_k\right) \tag{6}$$

$$\dot{\vec{R}}_{k+1} + \dot{\rho}_{k+1}\vec{p}_{k+1} + \rho_{k+1}\dot{\vec{p}}_{k+1} = \dot{f}_k\left(\vec{R}_k + \rho_k\vec{p}_k\right) + \dot{g}_k\left(\dot{\vec{R}}_k + \dot{\rho}_k\vec{p}_k + \rho_k\dot{\vec{p}}_k\right) \tag{7}$$

Copyright © 2020 Advanced Maui Optical and Space Surveillance Technologies Conference (AMOS) – www.amostech.com

$$p_{sr} = \frac{|\vec{r}_1 \times \dot{\vec{r}}_1|^2}{\mu} \tag{8}$$

$$\delta\nu = \arccos\left(\frac{\vec{r}_1 \cdot \vec{r}_2}{|\vec{r}_1||\vec{r}_2|}\right) \tag{9}$$

$$g = \frac{|\vec{r}_1||\vec{r}_2|\sin\delta\nu}{\sqrt{\mu p_{sr}}} \tag{10}$$

$$f = 1 - \frac{|\vec{r}_2|}{p_{sr}(1-\cos\delta\nu)} \tag{11}$$

$$\dot{g} = 1 - \frac{|\vec{r}_1|}{p_{rs}(1-\cos\delta\nu)} \tag{12}$$

$$\dot{f} = \frac{f\dot{g}-1}{g} \tag{13}$$

The terms containing either $\rho$ or $\dot{\rho}$ can be collected onto one side of each of these equations as shown in equations (14) and (15).

$$\rho_{k+1}\vec{p}_{k+1} - f_k\rho_k\vec{p}_k - g_k\dot{\rho}_k\vec{p}_k - g_k\rho_k\dot{\vec{p}}_k = f_k\vec{R}_k + g_k\dot{\vec{R}}_k - \vec{R}_{k+1} \tag{14}$$

$$\dot{\rho}_{k+1}\vec{p}_{k+1} + \rho_{k+1}\dot{\vec{p}}_{k+1} - \dot{f}_k\rho_k\vec{p}_k - \dot{g}_k\dot{\rho}_k\vec{p}_k - \dot{g}_k\rho_k\dot{\vec{p}}_k = \dot{f}_k\vec{R}_k + \dot{g}_k\dot{\vec{R}}_k - \dot{\vec{R}}_{k+1} \tag{15}$$

The range and range rate terms can then be pulled out to reform these two equations into a single system of equations in a matrix form. This system of equations for the two observation case with both angles and angle rates is shown in equation (16). Note that the zero in the upper right corner of the matrix is represented as a vector since it represents a column of three zeros.

$$\begin{bmatrix} -f_1\vec{p}_1 - g_1\dot{\vec{p}}_1 & -g_1\vec{p}_1 & \vec{p}_2 & \vec{0} \\ -\dot{f}_1\vec{p}_1 - \dot{g}_1\dot{\vec{p}}_1 & -\dot{g}_1\vec{p}_1 & \dot{\vec{p}}_2 & \vec{p}_2 \end{bmatrix} \begin{bmatrix} \rho_1 \\ \dot{\rho}_1 \\ \rho_2 \\ \dot{\rho}_2 \end{bmatrix} = \begin{bmatrix} f_1\vec{R}_1 + g_1\dot{\vec{R}}_1 - \vec{R}_2 \\ \dot{f}_1\vec{R}_1 + \dot{g}_1\dot{\vec{R}}_1 - \dot{\vec{R}}_2 \end{bmatrix} \tag{16}$$

Just as the original least squares algorithm by Karimi and Mortari could be adapted to accept additional measurements beyond the three required, this angles and angle rates approach can be adapted to accepts more than two measurements. The relationship between the first and second measurement as shown in equation (16) defines the relationship between any pair of measurements. The same calculation can be performed with multiple observations beyond the initial two by extending the matrices in equation (16) with shifted forms identical to the relationship between the first and second measurements. The general form for a case with $n$ measurements is shown in equation (17).

Copyright © 2020 Advanced Maui Optical and Space Surveillance Technologies Conference (AMOS) – www.amostech.com

$$
M = \begin{bmatrix}
-f_1\vec{p}_1 - g_1\dot{\vec{p}}_1 & -g_1\vec{p}_1 & \vec{p}_2 & \vec{0} & \vec{0} & \vec{0} & \dots \\
-\dot{f}_1\vec{p}_1 - \dot{g}_1\dot{\vec{p}}_1 & -\dot{g}_1\vec{p}_1 & \dot{\vec{p}}_2 & \vec{p}_2 & \vec{0} & \vec{0} & \dots \\
\vec{0} & \vec{0} & -f_2\vec{p}_2 - g_2\dot{\vec{p}}_2 & -g_2\vec{p}_2 & \vec{p}_3 & \vec{0} & \dots \\
\vec{0} & \vec{0} & -\dot{f}_2\vec{p}_2 - \dot{g}_2\dot{\vec{p}}_2 & -\dot{g}_2\vec{p}_2 & \dot{\vec{p}}_3 & \vec{p}_3 & \ddots \\
\vdots & \vdots & \vdots & \vdots & \vdots & \vdots & \vdots \\
\vec{0} & \dots & \vec{0} & -f_{n-1}\vec{p}_{n-1} - g_{n-1}\dot{\vec{p}}_{n-1} & -g_{n-1}\vec{p}_{n-1} & \vec{p}_n & \vec{0} \\
\vec{0} & \dots & \vec{0} & -\dot{f}_{n-1}\vec{p}_{n-1} - \dot{g}_{n-1}\dot{\vec{p}}_{n-1} & -\dot{g}_{n-1}\vec{p}_{n-1} & \dot{\vec{p}}_n & \vec{p}_n
\end{bmatrix}
$$

$$
\vec{x} = \begin{bmatrix} \rho_1 \\ \dot{\rho}_1 \\ \rho_2 \\ \dot{\rho}_2 \\ \rho_3 \\ \dot{\rho}_3 \\ \vdots \\ \rho_n \\ \dot{\rho}_n \end{bmatrix}
\qquad
\vec{\xi} = \begin{bmatrix}
f_1\vec{R}_1 + g_1\dot{\vec{R}}_1 - \vec{R}_2 \\
\dot{f}_1\vec{R}_1 + \dot{g}_1\dot{\vec{R}}_1 - \dot{\vec{R}}_2 \\
f_2\vec{R}_2 + g_2\dot{\vec{R}}_2 - \vec{R}_3 \\
\dot{f}_2\vec{R}_2 + \dot{g}_2\dot{\vec{R}}_2 - \dot{\vec{R}}_3 \\
\vdots \\
f_{n-1}\vec{R}_{n-1} + g_{n-1}\dot{\vec{R}}_{n-1} - \vec{R}_n \\
\dot{f}_{n-1}\vec{R}_{n-1} + \dot{g}_{n-1}\dot{\vec{R}}_{n-1} - \dot{\vec{R}}_n
\end{bmatrix}
$$

$$
M\vec{x} = \vec{\xi} \tag{17}
$$

Variables can be used to stand in for the matrix and vectors and the full system can be rewritten as a single linear equation of the form shown in equation (17) where $M$ is the matrix, $\vec{x}$ is the vector of ranges and range rates, and $\vec{\xi}$ is the remaining vector. For a given series of measurements of the same space object, the least-squares solution for $\vec{x}$ can be found by taking the Moore-Penrose inverse of $M$ and post-multiplying it by $\vec{\xi}$. These range and range rate values can be plugged back in to recalculate the Lagrange coefficients and therefore the elements of $M$ and $\vec{\xi}$. In the results section of this paper, it is shown that for an initial choice of zero for all ranges and range rates, this iterative least-squares converges to the correct solution in most cases. It is essential to remember that the initial assumption of zero only goes into finding the Lagrange coefficients for constructing the terms of $M$ and $\vec{\xi}$. The first value of $\vec{x}$ is calculated from these terms and not initially assumed to be the zero vector.

### 2.3 Particle Swarm Optimization

The iterative least-squares method for estimating a full orbit state from angle and angle rate measurements correctly finds the solution in many cases. However, convergence is not guaranteed, and there are cases where it fails such as those where the observer and target are both in or nearly in geostationary orbits. In order to approach the problem more rigorously, the least-squares method can be reformulated into a cost function. This will allow for new strategies for finding the target's state in addition to the iterative least-squares approach discussed previously.

First, rather than making an assumption about the ranges and range rates to inform the elements of $M$ and $\vec{\xi}$ and then finding $\vec{x}$ from this, the values for the ranges and range rates at each measurement are set to be the same in all of the terms. Equation (17) can be rewritten as a cost function by placing all of the terms on one side of the equation and recognizing that the difference of $M\vec{x}$ and $\vec{\xi}$ will only be the zero vector when a valid set of ranges and range rates are used to build all three variables. Accordingly, the difference of these terms will be non-zero for any solution that does not meet the constraints of the dynamical system. A single cost can be derived from this by taking the 2-norm of the difference. To balance the impact of inaccurate position and velocity states, a weighting matrix can be used to pre-multiply the difference vector before taking the norm. This weighting matrix is chosen to balance the impact of each component on the total cost. In Earth cononical units, the identity matrix is sufficient as the position and velocity components are similar in scale. In metric, choosing velocity weights of one thousand and positional weights of one can balance out the one thousand to one ratio between the scale of typical orbital radii and orbital velocities. The odd rows of the difference vector correspond to position errors while the even rows correspond to velocity errors. Weights can be chosen based on any prior knowledge of the target object's state. Alternatively, working in canonical units can account for much of the difference with unity weightings. The cost function with some diagonal weight matrix $W$ is provided in equation (18). Independent of the choice for $W$, the cost is still zero if the solution is exact.

Copyright © 2020 Advanced Maui Optical and Space Surveillance Technologies Conference (AMOS) – www.amostech.com

$$f = |W(M\vec{x} - \vec{\xi})| \tag{18}$$

With the problem rewritten as a cost function, a number of new approaches open up. One of the approaches is to perform a particle swarm optimization over the space of possible ranges and range rates. A particle swarm optimization starts with some number of randomly or strategically placed particles spread out through the solution space of a cost function. Each step of the algorithm has the particles move in a random direction with probabilities weighted by both the minimum value the particle has encountered on the cost function as well as the minimum value found by any particle in the swarm. As the algorithm continues, particles are drawn to the global minimum so long as at least one particle has begun to explore the region around the global minimum. As more particles are pulled into this well, they are able to explore it more thoroughly with each iteration. There are a number of tunable parameters that define both how quickly the algorithm converges and how likely it is to fail and miss the global minimum.

The most direct implementation would be to perform a particle swarm optimization over a space with dimension equal to the number of elements in $\vec{x}$ in order to have a term for the range and range rate for each measurement. In its most basic form, the bounds on the particle swarm could be set to safe feasible limits with a maximum range of perhaps twice the Earth's Hill sphere and range rate of several kilometers per second to match.

However, admissible regions can be applied to give much tighter constraints on both of these limits. Applying admissible regions requires some basic assumptions about the target object's state, but they significantly reduce the feasible solution space. For tracking expected Earth-orbiting satellites, the target can be assumed to be in an elliptical orbit that does not impact the Earth. This provides constraints in the object's semi-major axis, orbital eccentricity, and radius of periapse.

Another tool for significantly constraining the solution space is to only find the range and range rate for a single observation and project this state to the other observation times to find their corresponding ranges and range rates from this assumption. This reduces the dimension of the solution space to two with one dimension corresponding to range and the other range rate for the first observation. This is possible since the measured heading and heading rate with a selected range and range rate fully defines the state at a time, and future states can be estimated by propagating the orbit forward in time by solving Kepler's equation. While there is no analytical solution to Kepler's equation (19), applying a root-finding algorithm due to Laguerre can find the solution to machine precision with only a few iterations [3].

$$M = E - e\sin E \tag{19}$$

When an erroneous estimated state is projected to future times, the expected measurement of the projected state may not match the measured heading and heading rate. The simplest implementation of the cost function can ignore this error since erroneous states will be penalized in equation (18). However, it is also reasonable to find the angular distance between the observed and expected measurement and incorporate this difference into a new cost function that penalizes both error in equation (18) and error in the expected measurement. The contours of the solution space can be manipulated by choosing weights for each of these terms. An alternative cost function of this form is provided in equation (20). Errors for both the forward and backward projection of a chosen range and range rate are included for each measurement and the user-defined weightings are labeled as $w_i$. The predicted headings are denoted as $\hat{p}_i$.

$$f = \sum_{i=2}^{n} w_i \arccos(\hat{p}_i \cdot \vec{p}_i) + |W(M\vec{x} - \vec{\xi})| \tag{20}$$

Implementing a particle swarm optimization over the higher dimensional solution space would have been prohibitively costly in terms of computational resources. The number of particles required to search the solution space grows exponentially with the number of dimensions in the solution space [16]. With this reduced two-dimensional solution space, a particle swarm optimization can be run with much greater efficiency. Furthermore, the admissible region constraints can provide fairly tight bounds on this two-dimensional solution space depending on how much information the designer is able to assume. By using a universal variable formulation for both the Kepler's problem solver and in the derivation of the cost function itself, the approach does not need to assume a closed elliptical orbit. Rather, this method can be used to perform initial orbit determination on orbits corresponding to any conic section.

Copyright © 2020 Advanced Maui Optical and Space Surveillance Technologies Conference (AMOS) – www.amostech.com

### 2.4 Nelder-Mead Optimization

With the cost function approach to initial orbit determination discussed in the previous section, any derivative-free optimization method can be applied to solve the problem. One particularly attractive alternative to the particle swarm optimization is the Nelder-Mead simplex-based approach [13]. In the case of a two-dimensional state space, the Nelder-Mead algorithm tracks the values reported by three points as they explore the cost function space. The simplex formed by these three points is manipulated by repositioning the three vertices through a method that brings the simplex as close as possible to the a minimum.

The method stats with the initial placement of the three vertices in the state space. A-priori knowledge regarding the likely state of the target can be used to choose an intelligent start point. In this case, the vertices should surround the minimum to maximize the likelihood that the optimizaer will converge [12]. With no a-priori knowledge, the vertices can be chosen randomly. The implemented method assumes nothing and selects random states for each vertex. The cost for each vertex is checked, and vertices outside of the bounnds of the penalty function are re-selected until a point inside the bounds of the penalty function is found.

In each iteration of the algorithm, the costs at each of the vertices and a point projected outside of the simplex and inside the simplex are compared. The vertex with the highest cost is moved to one of these new points, and the process is repeated until the simplex converges down to a minimum [10]. In order to ensure that the algorithm converges to the correct minimum, the full process is repeated several times. The algorithm exits when it finds a point with sufficiently low cost or after it hits a maximum number of iterations and returns the state with the lowest cost on any iteration. Repeating the full algorithm allows for multiple opportunities to generate an appropriate set of initial conditions so that the encountered minimum is the unique global minimum that corresponds to the solution.

## 3. RESULTS

### 3.1 Solution Space

Restructuring the initial orbit determination algorithm as a cost function opens the question of what form the solution space takes. This includes the number of minima that an optimization method might find in addition to the true solution. These additional convex regions of the cost function could serve to draw away an optimization algorithm from the true solution and have it report erroneous results. Similarly, there is the question of how deep these minima go. The cost function is designed to return zero for a solution that perfectly matches the observed measurements and dynamics. If the other minima are significantly above zero, this could be integrated into the optimization algorithm so that it can leave these regions if the local minimum does not approach a sufficiently small value. Beyond these two quantifiable measures of the solution space, the contours of the cost function can show if in some cases the minimum is not unique in the case of degenerate observations.

Figures 1 through 6 show the contours generated by the the two cost functions for a variety of scenarios. The first cost function is referred to as the projection cost function. This cost is based on taking the first measurement and an a range and range rate guess. This forms a full state estimate that is projected forward in time to the time of the second measurement. The cost is then taken as the angular error between the angle measurement at this second time and the expected measurement based on the range and range rate guess. The process is repeated with the second measurement projected back in time to the first measurement. These errors are added together to give the estimate's cost. The second cost function is the $L_n$+Rates cost function developed in the Theory section. A penalty function based on admissible regions is added to both of these cost functions. The admissible regions penalty function takes in the state estimate and checks that the range, range rate, radius of periapse, semi-major axis, and eccentricity are valid based on what is known about the system. For these figures, the bounds are set to require that the target is orbiting the Earth without impacting it and the eccentricity is below 0.2. To ensure a smooth transition between penalized regions and non-penalized regions, the penalty function takes an exponential form.

When a state estimate falls outside the bounds defined by the penalty function, the difference between the state and the bound is multiplied by a weight to increase the penalty associated with erroneous eccentricities and velocities and balance them with the penalty for out of bounds ranges and semi-major axes. For Earth-orbiting satellites in metric units, distances tend to be about three orders of magnitude larger than velocities and velocities tend to be at least an order of magnitude greater than eccentricity. This acts as a guide for choosing weights so as not to allow errors of one type dominate the others. The penalty is taken as the exponential of the sum of these weighted errors. One is then

Copyright © 2020 Advanced Maui Optical and Space Surveillance Technologies Conference (AMOS) – www.amostech.com

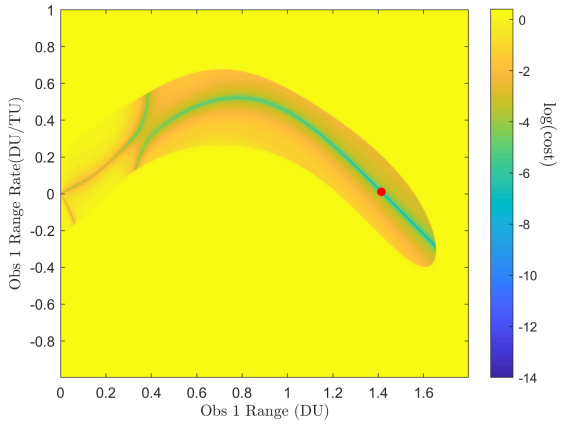


Fig. 1: LEO observer to LEO target measurement error log(cost) contours.

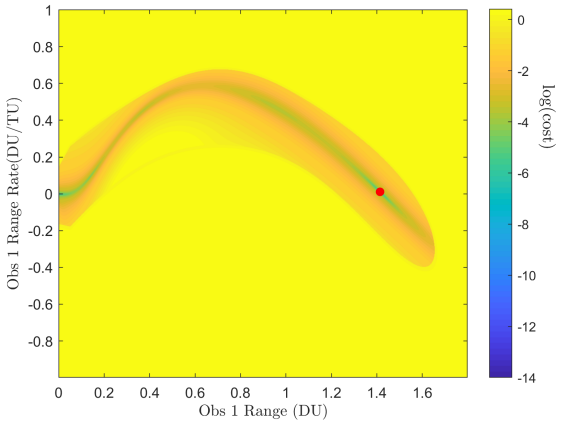


Fig. 2: LEO observer to LEO target $L_n$+Rates log(cost) contours.

subtracted from the result so that the penalty is zero when all terms are within their respective bounds. The exponential form ensures that estimates that are far out of bounds are appropriately penalized.

### 3.1.1 Non-Coplanar Case

The four investigated cases correspond to all combinations of geosynchronous and low-Earth orbiting observers and targets in the single-revolution case. A red dot is placed on the image where the true solution is located. The LEO orbit for both the target and the observer is based on a nearly circular orbit near-equatorial orbit. Specifically, the orbit is at an altitude of 400 kilometers and the inclination is zero for the observer and 10 degrees for target. The geosynchronous orbit is defined as one with a semi-major axis of 42164 kilometers and a identical approach of zero degrees for the observer and 10 degrees for the target object. This prevents the case from being coplanar. The coplanar case is developed in the following section.

The penalty bounds determine the overall shape of the investigated region. In the case where both the observer and target are in a low-Earth orbit, the feasible states are confined to a crescent in range and range-rate space. A valley of low cost runs through this crescent. However, for the non-coplanar case, the cost only reaches zero for a unique non-trivial point that corresponds to the correct range and range-rate. The responses for both cost functions are similar, however, the exact line traced out by this valley is shifted for each case. In the projection error case, there are two distinct curves that form the cost valleys. In the $L_n$+rates function, there is a single valley that winds through the feasible region.

For the case where both the observer and target are confined to geosynchronous orbits, the crescent shape remains, but a small circular region with negative range-rate opens up with no penalty. However, this local minimum remains well above the global minimum still confined to the crescent region. Once again, this structure is similar for both cost functions. One detail that differs is the cost function response near the trivial solution. This is zero in both cases. However, in the projection case, this point around rise faster than in the $L_n$+Rates case.

The two remaining cases are for observers and targets in different orbits. In both of these cases, three distinct local minima show up. One is about the trivial solution, while the other two are non-trivial. Similar to the double geosynchronous case, one of these is a local minimum that does not fall to the global minimum found only at the correct solution and the trivial solution. Figures 5 and 6 show the LEO to GEO scenario. The GEO to LEO scenario is not shown. However, it is structurally similar to the LEO to GEO scenario. The main differences are small changes in the shape to the penalty function bounds and the location of the solution within the solution space.

Copyright © 2020 Advanced Maui Optical and Space Surveillance Technologies Conference (AMOS) – www.amostech.com

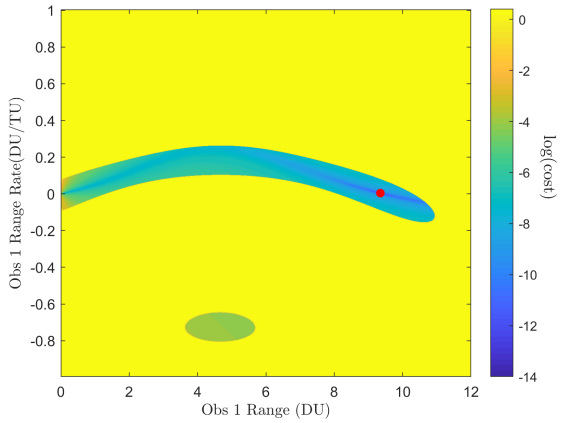


Fig. 3: GEO observer to GEO target measurement error log(cost) contours.

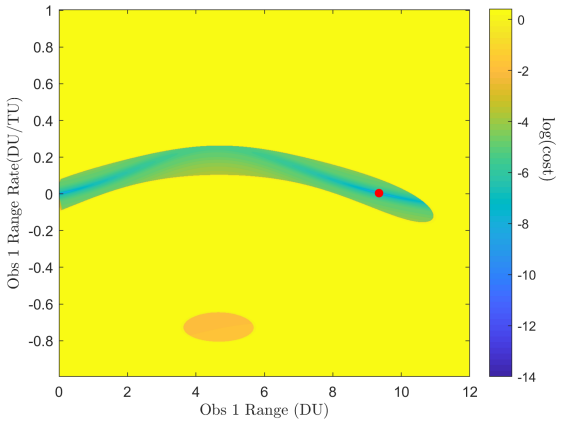


Fig. 4: GEO observer to GEO target $L_n$+Rates log(cost) contours.

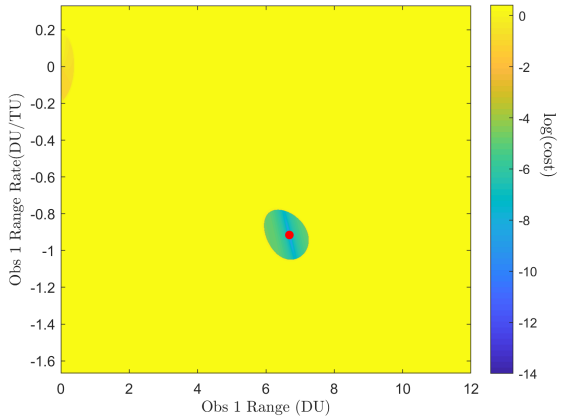


Fig. 5: LEO observer to GEO target measurement error log(cost) contours.

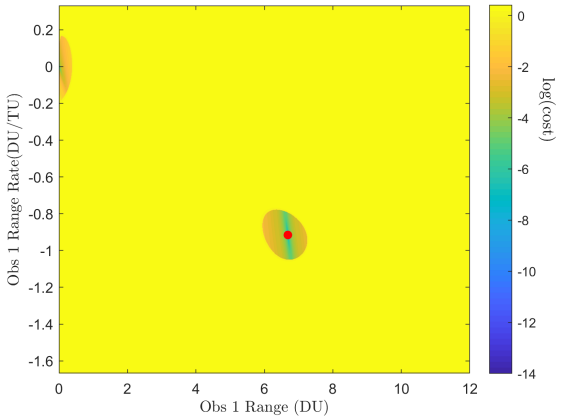


Fig. 6: LEO observer to GEO target $L_n$+Rates log(cost) contours.

Copyright © 2020 Advanced Maui Optical and Space Surveillance Technologies Conference (AMOS) – www.amostech.com

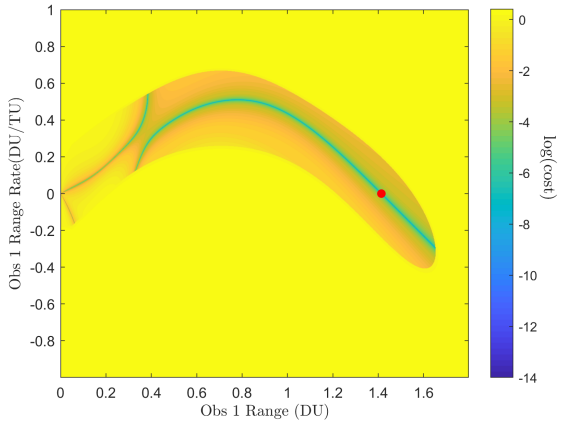


Fig. 7: Coplanar LEO observer to LEO target measurement error log(cost) contours.

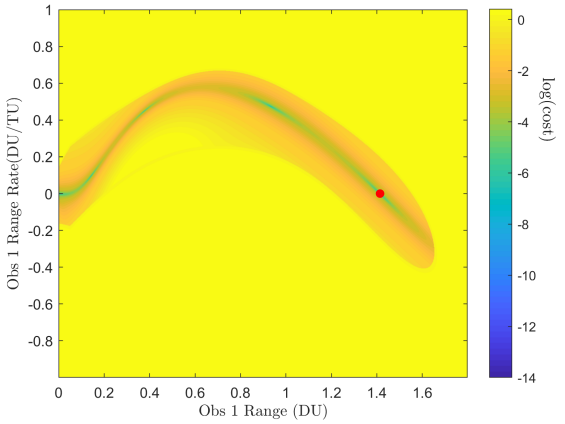


Fig. 8: Coplanar LEO observer to LEO target $L_n$+Rates log(cost) contours.

### 3.1.2 Coplanar Case

The inclination of the second object is zeroed out for the LEO observer and LEO target case. While this does not significantly shift the over-all shape of the permissible region as defined by the admissible region penalty function, this does change the geometry of the contours inside the permissible region. The projection-based cost function shows two curves of zeroes in the cost function, and as a result, the global minimum is no longer the unique solution. However, the $L_n$+Rates cost function does not face this same issue. In the coplanar case, the $L_n$+Rates cost crescent contains a unique global minimum and two additional non-trivial local minima. Since both cost functions correctly return zero for the correct solution, they can be combined together to generate a new cost function with the benefits of both geometries. The result for this combined cost function for the same LEO to LEO case is shown in figure 9. This function keeps the unique global minimum in the coplanar case from the $L_n$+Rates cost function and the favorable geometry around the trivial zero from the projection cost function. This favorable geometry keeps the cost around the trivial solution higher to help push the optimization function away. The trivial solution can be manually excluded using the admissible regions limits. However, the projection cost function helps keep this bound less attractive for the optimization algorithm.

The geometry for this combined cost function is favorable in many cases, but it is not guaranteed as the relative positions of the projection and $L_n$+rates cost function minima shift for different orbit scenarios. In some cases, the combined cost function contours remains more similar to that of the target measurement error alone contours. In these cases, while there may still remain an objective minimum, the long and shallow valley that contains it may also have other local minima that confound both the particle swarm and Nelder-Mead approaches as they descend. For one thousand Monte-Carlo simulated cases of coplanar LEO to LEO observations, 58.4 percent of the cases converged to the correct state. These were generated with the values in table 1.

Similar to the LEO observer and LEO target case, the Geostationary observer and target case does not have a unique solution for either the measurement projection or $L_n$+rates cost function. The curves are similar in structure to those for the LEO case. However, the $L_n$+rates case has shifted from several discrete minima to a continuous curve of minima as shown in figure 11. When the two cost functions are summed, the unique non-trivial intersection of these curves of minima align with the true solution to the problem. In the geostationary case as well, the combined cost function can provide the unique correct answer to the orbit determination problem. This occasionally suffers from the same issue of poor cost function geometry. For one-thousand Monte-Carlo simulated cases with the cases based on the values from table 1, 84.7 percent converged to the correct solution.

## 3.2 Simulated Test Cases

A Monte Carlo method is applied to test the developed initial orbit determination methods under a variety of scenarios. Both the particle swarm approach as well as the Nelder-Mead algorithm are tested. Each one is run with the same set of one thousand observer and target pairs by generating the cases with a seeded random number generator. The same

Copyright © 2020 Advanced Maui Optical and Space Surveillance Technologies Conference (AMOS) – www.amostech.com

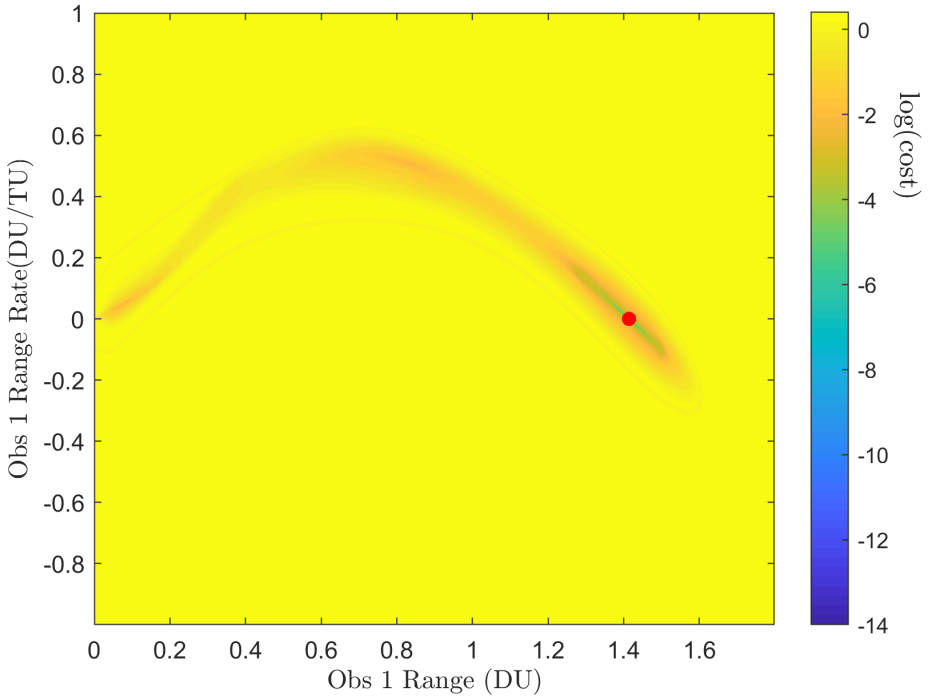


Fig. 9: Coplanar LEO observer to LEO target log sum of the two cost functions.

four scenarios as investigated in the cost function contour study are used again. That is each possible combination of low-Earth and geosynchronous orbits to see how each domain responds to both algorithms.

The Monte-Carlo randomly generated observer and target orbits using the values from the table below. The values with means and standard deviations are generated from a normal distribution. The terms with a minimum and maximum are generated using a uniform distribution. The results of all the cases are plotted in a series of scatter plots. Figure 13 shows the results for the particle swarm applied to the LEO observer and LEO target and figure 14 for the Nelder-Mead algorithm.

The x-axis for the scatter plots is the time in Earth canonical time units (TU) between the first and second observation. One TU is equivalent to 806.8042 seconds. This comes from the mean motion of a theoretical orbit at the surface of the Earth. The y-axis results on each scatter plot is the time in seconds required to find the solution for each case. In both algorithms, this value is highly dependent on chosen parameters that balance the algorithm's ability to converge to the correct solution with the time required to compute the result. Finally, the color and shape of the point on the scatter plot corresponds to whether the estimated state matched the true state to within one percent in all six translational state components. The gray squares had at least one state component that did not match the true state to within one percent. The blue circles represent estimated states that correctly match the true state on all components to one percent.

Both the particle swarm and Nelder-Mead methods converge toward a solution as they iterate. However, in a practical implementation there will be measurement error in the angle and angle rate data that the algorithm ingests. This makes it impractical to define a convergence criterion based on some minimum value for the cost function. Due to this, the global minimum of the solution space may never reach a hard-coded stopping point and the algorithm would not be able to adjust to different levels of certainty in the input measurements. To account for this, the convergence criteria can be defined with the Mahalanobis distance. Either algorithm can accept a measurement covariance matrix input. The Mahalanobis distance is found by using the current estimate of the range and range rate states to find a full state. This is then projected to the times of the two measurements and an expected measurement is generated. The expected measurement, $\hat{y}$, can then be compared with the input measurement, $\vec{y}$, and the error between these two states can be applied to the Mahalanobis distance equation shown in equation (21) where $S$ is the measurement covariance matrix.

Copyright © 2020 Advanced Maui Optical and Space Surveillance Technologies Conference (AMOS) – www.amostech.com

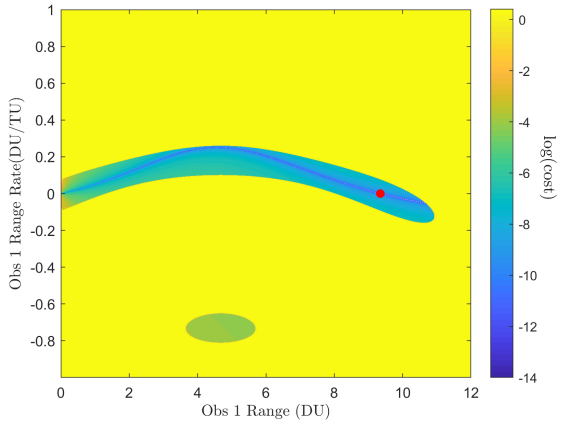


Fig. 10: Coplanar GEO to GEO measurement error log(cost) contours.

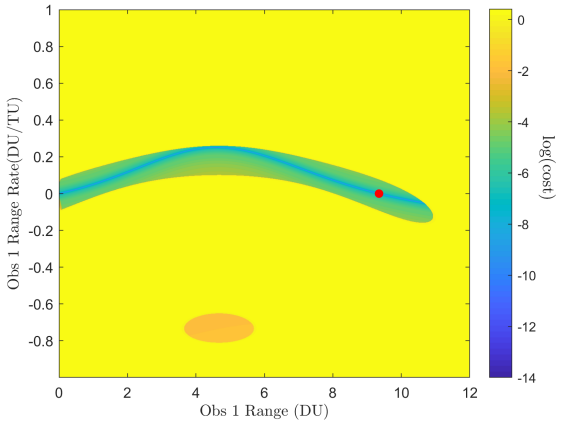


Fig. 11: Coplanar GEO to GEO $L_n$+Rates log(cost) contours.

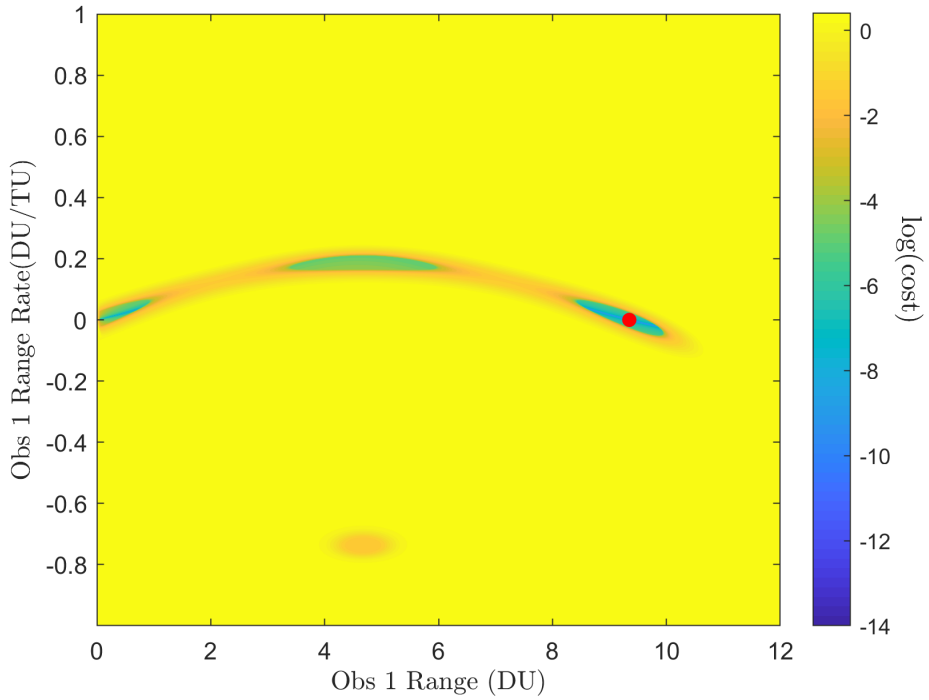


Fig. 12: Coplanar GEO observer to GEO target log sum of the two cost functions.

$$m = \sqrt{(\vec{y} - \hat{y})^T S^{-1} (\vec{y} - \hat{y})} \tag{21}$$

Four scenarios are investigated and the results are summarized in figures 15 through 16. Figure 15 shows the ratio of correct results, defined as all state components with less than one percent error. The Nelder-Mead algorithm more consistently converges to the true state in all cases. It's performance is worst with the LEO-LEO scenario. As shown in figure 14, this is due to the high error rate as the time between observations increases to the point that both objects have moved a significant fraction of an orbit. Figure 16 shows the calculation time distribution for all scenarios for the two algorithms. The box and whisker plots show that the Nelder-Mead algorithm is much more consistent in the time

Copyright © 2020 Advanced Maui Optical and Space Surveillance Technologies Conference (AMOS) – www.amostech.com

| Type | $a$ Mean | $a$ STD | $e$ Max | $i$ Mean | $i$ STD | $\Omega/\omega/\nu$ Min | $\Omega/\omega/\nu$ Max | $\Delta t$ Min | $\Delta t$ Max |
|---|---|---|---|---|---|---|---|---|---|
| LEO | 8413 km | 100 km | 0.001 | 0° | 45° | 0° | 360° | 0 s | 3600 s |
| GEO | 42164 km | 100 km | 0.001 | 0° | 7° | 0° | 360° | 0 s | 3600 s |

Table 1

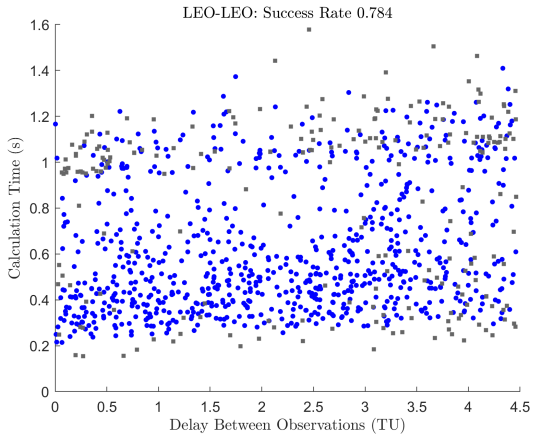


Fig. 13: LEO observer to LEO target Monte Carlo particle swarm Results.

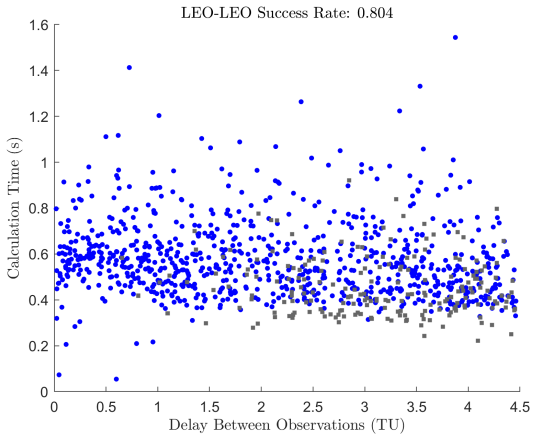


Fig. 14: LEO observer to LEO target Monte Carlo Nelder-Mead Results.

required to find a solution. The average computation time is lower for the Nelder-Mead algorithm.

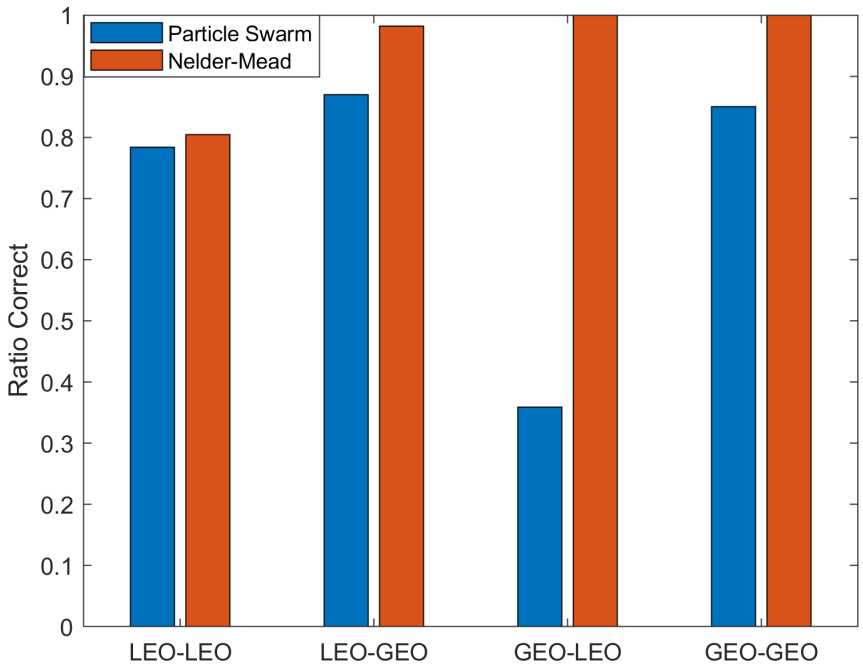


Fig. 15: Ratio of correct solutions for both the particle swarm and Nelder-Mead approaches.

For the previous test cases with the Nelder-Mead algorithm, the maximum number of initializations per case is set

Copyright © 2020 Advanced Maui Optical and Space Surveillance Technologies Conference (AMOS) – www.amostech.com

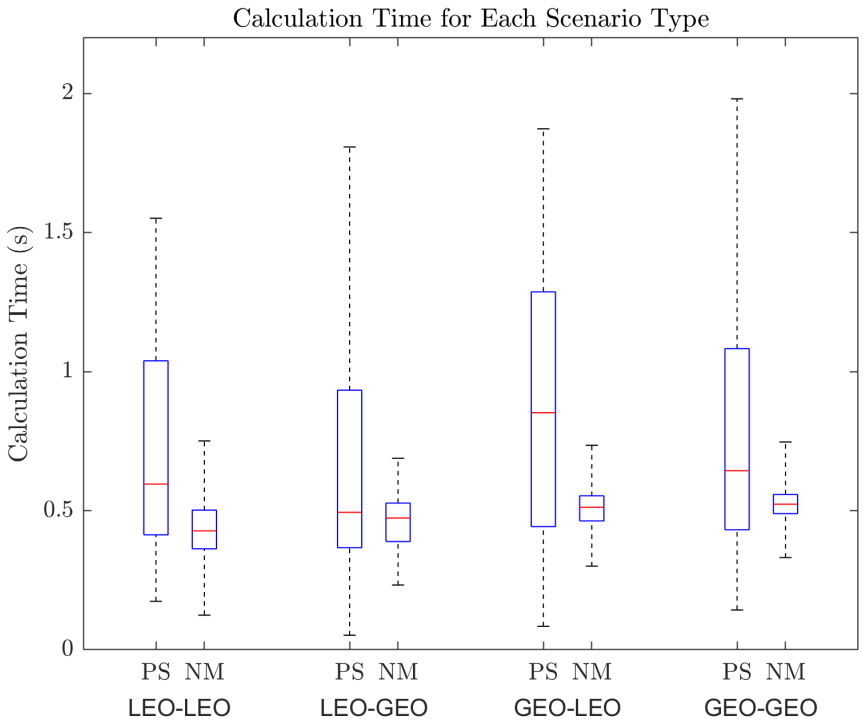


Fig. 16: Particle swarm (PS) and Nelder-Mead (NM) computation time by scenario. The whiskers show the maximum and minimum while the box shows the twenty-fifth percentile, mean, and seventy-fifth percentile [4].

to fifty. However, there is a trade-off between computation time and accuracy where the more times the algorithm is reinitialized with new randomly generated initial conditions, the more opportunities there are for the algorithm to converge to a global minimum and the more time there is potentially spent on each case. This trade-off is investigated by running the same set of one-thousand cases with several different values for the maximum number of runs. The results for both the accuracy of the solutions and the average time per case are shown in figures 17 and 18 respectively. The accuracy shows a steep rise as the maximum number of runs increases up to fifteen followed by a sharp leveling off. After this point, more runs gradually increase the method's accuracy, but the change is under a percent between fifteen up to fifty. The time cost shows a much more linear result. The computation time increases steadily as the maximum number of iterations increases. The linear least squares fit for this line has a slope of 0.007844 seconds per run, and the coefficient of determination for the fit is 0.9902.

### 3.3 Multi-Orbit Scenario

All of the previous simulations for the developed initial orbit determination algorithms have assumed that the time between observations was less than a full period of either the observer or target object's orbit. However, if the time between observations is sufficiently large, it becomes feasible that the target or observer has completed more than a full revolution around the Earth. The developed algorithms remain functional even in this case. There is no longer a unique solution for the case of two observations. Figure 19 shows the summed cost function contours for a LEO observer and LEO target case with a thirty-thousand second delay between the two angles and angle rates observations. The penalty function retains its shape, but the interior is divided into a series of curves. Each of these curves represents a feasible solution given the available data. The plot has several distinct non-trivial global minima, and only the correct solution is marked with a red dot. Accordingly, a single solution is not sufficient to characterize the set of global minima of this cost function.

With some light edits, the Nelder-Mead approach can be altered to report all identified minima, and the accuracy of the method can be measured by checking if the true state is in the set of reported solutions. With this modification, figure 20 shows the scatter plot results for a LEO observer and LEO target object with time delay between observations up to thirty-thousand seconds. The accuracy of the algorithm falls as the time delay increases.

Copyright © 2020 Advanced Maui Optical and Space Surveillance Technologies Conference (AMOS) – www.amostech.com

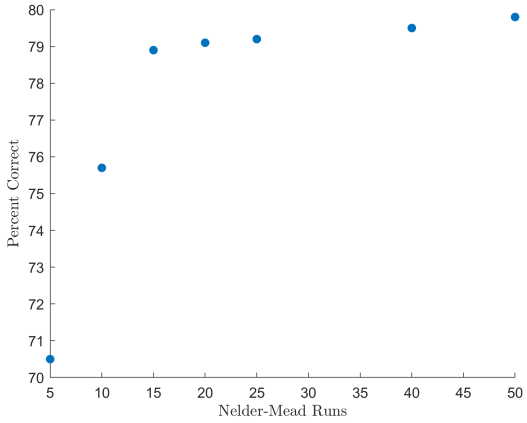


Fig. 17: LEO observer to LEO target percent correct as a function of the number of Nelder-Mead runs.

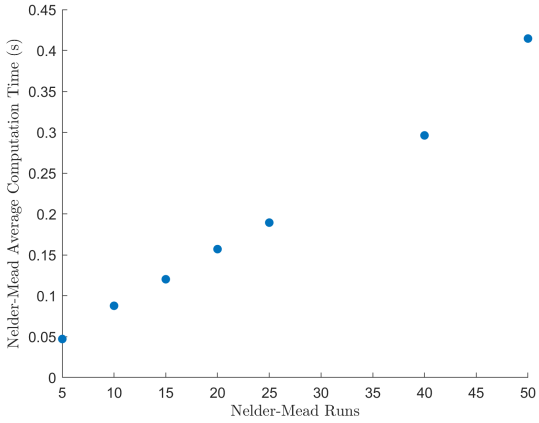


Fig. 18: LEO observer to LEO target average computation time as a function of the number of Nelder-Mead runs.

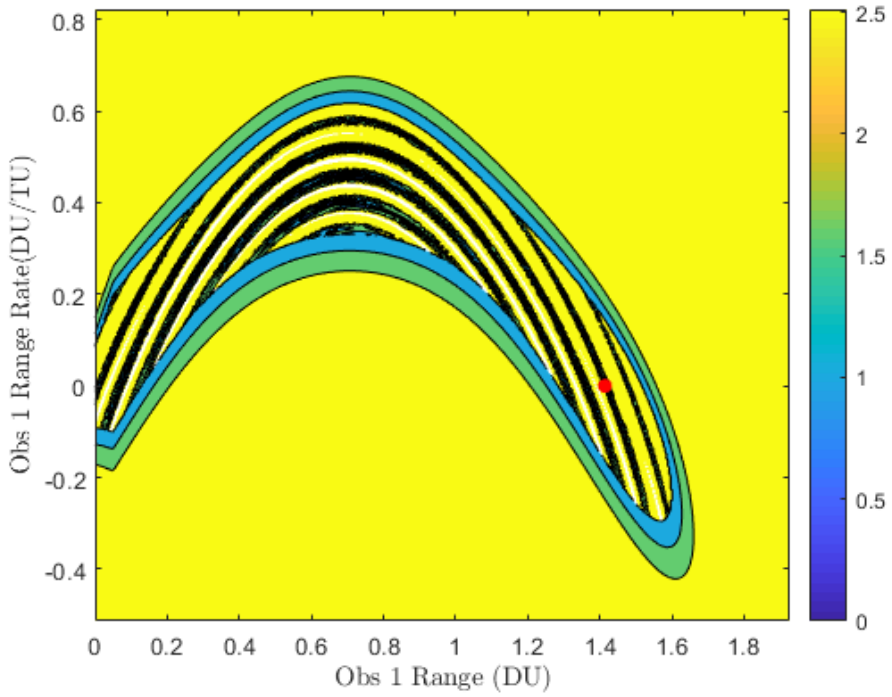


Fig. 19: LEO observer to LEO target Multi-Revolution cost function contours.

### 3.4 Empirical Verification

To verify that the Nelder-Mead algorithm could accurately estimate the translational state of actual spacecraft. The algorithm is empirically verified on a series of images taken of actual Earth-orbiting space objects. The images are taken with the Omnidirectional Space Situational Awareness Telescope (OmniSSA) at the University of Colorado at Boulder. This imaging system is composed of four all-sky cameras with overlapping fields of view to improve the effective signal to noise ratio. The boresights of the cameras are fixed with respect to the ground, so non-geostationary space objects appear to streak through the frame for longer integration times. Two observation runs are included in the results. The first took place in the evening of October fourth, 2018, and the second was on November eighth, 2019.

Copyright © 2020 Advanced Maui Optical and Space Surveillance Technologies Conference (AMOS) – www.amostech.com

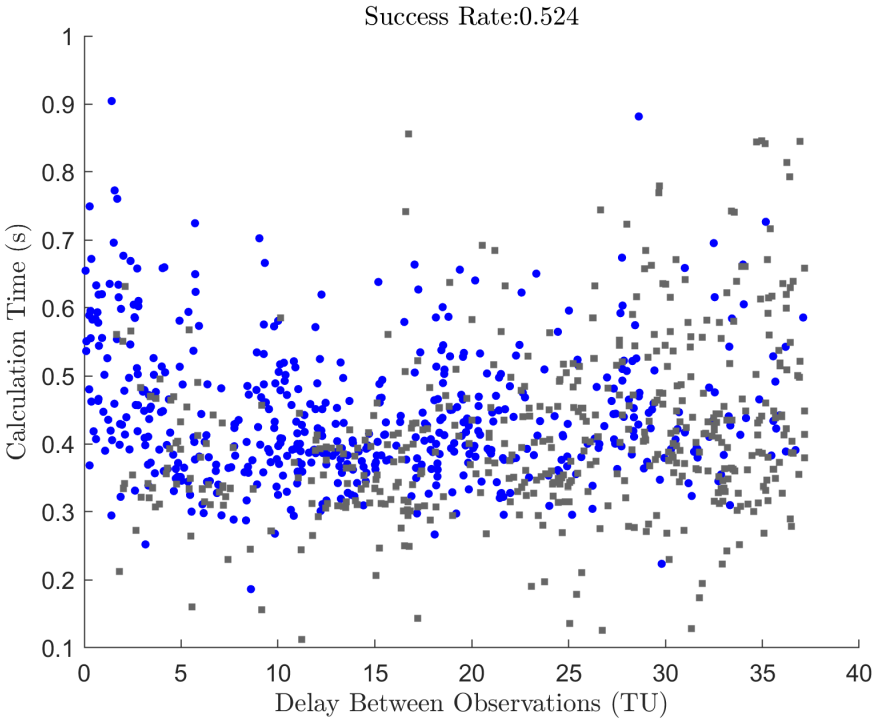


Fig. 20: LEO observer to LEO target Multi-Revolution Monte Carlo method.

In the first of these sessions, the integration time was set to seven seconds. In the latter, the integration time was ten seconds.

To determine the true orbits of the imaged objects, the two-line element (TLE) catalogs for all unclassified objects are collected for the period around each observation date. This data set is then narrowed down by removing multiple listings for the same object taken at different times. The retained TLE is the listing with the closest epoch to the actual observation time. The catalog data is obtained from Space-Track [1]. In order to determine which TLE's the objects correspond to, the TLE data is passed into the open source night sky visualizer Stellarium, that uses an SGP4 integrator to show the motion of the input objects as the simulated time changes [2]. The motion of the simulated satellites is compared to the observed objects. Associations are made by comparing the simulated and observed predicted positions at the time of the observation as well as the type of object the TLE represents in order to ensure the TLE object is bright enough to reasonably create the observed streak.

The right ascension and declination of the target object at the start and end of each streak are then found by determining their respective precise locations in the image frame and passing that through a custom MATLAB function. This function uses the boresight angles determined by the Astrometry.net software image calibrator [11]. The lens distortion is accounted for with a LOESS-based calibration algorithm. Combined together, these tools allow a user to determine the right ascension and declination from the observed pixel coordinates in an imaged frame.

The right ascension and declination is translated into a heading vector through equation (22). The angle rates are determined by finding the heading for both the start and end of the streak and assuming straight line motion on the surface of the celestial sphere to determine the heading rate through numerical differentiation. The observer position is found by converting the latitude, longitude, and altitude of the observer to Earth-centered, Earth-fixed coordinates and pre-multiplying this vector by a rotation matrix that is based on the observation time to translate these coordinates to the Earth-centered inertial frame. The observer velocity in the inertial frame can then be found via numerical differentiation through equation (23).

$$\vec{p} = [\cos\delta\cos\alpha, \cos\delta\sin\alpha, \sin\delta]^T \tag{22}$$

Copyright © 2020 Advanced Maui Optical and Space Surveillance Technologies Conference (AMOS) – www.amostech.com

| Target | Orbital Radius | Estimated Orbital Radius | Inclination | Estimated Inclination |
|---|---|---|---|---|
| Yaogan 3 | 7004 km | 6934 km | 98.0° | 102.6° |
| Kondor-E 1 | 6830 km | 7054 km | 74.7° | 66.0° |
| TUPAC KATARI | 42145 km | 43583 km | 0.06° | 0.86° |
| OAO 1 | 7156 km | 7292 km | 35.0° | 34.4 ° |
| SL-3 R/B | 6917 km | 6972 km | 81.2° | 86.3° |

$$^{\mathscr{N}}\dot{R} = \frac{[NR(t)][RN(t+\delta t)] - I_{3\times 3}}{\delta t}[NR(t)]^{\mathscr{R}}R \tag{23}$$

A table of the observed and expected results for a series of identified objects is provided. The expected and estimated orbital parameters

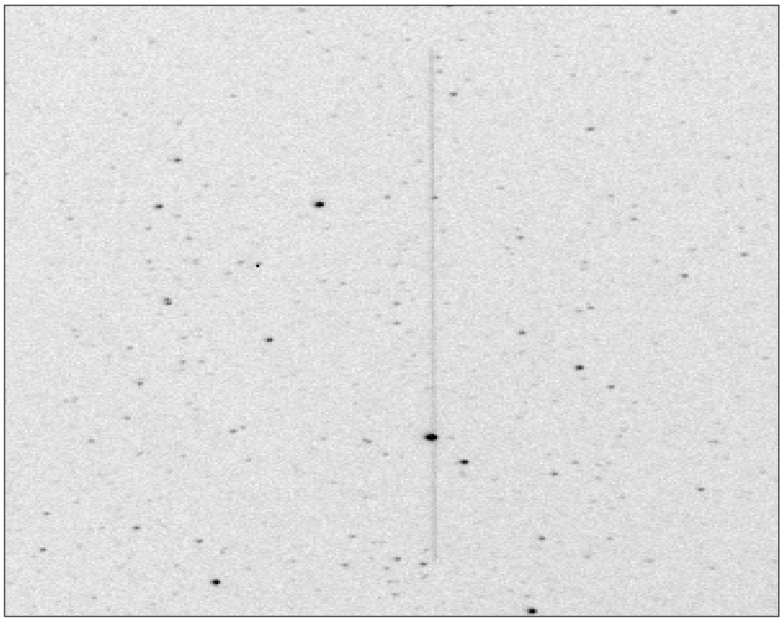

Fig. 21: Streak generated by the Yaogan 3 satellite over a 10 second integration.

## 4. CONCLUSION

A number of related developments on initial orbit determination have been formulated and discussed. First, a new method for initial orbit determination from angles and angle rates has been derived based on the $L_n$ method developed by Reza Raymond Karimi and Daniele Mortari. This method was investigated by itself then abstracted into a cost function to allow traditional derivative-free optimization to find an estimate for the true state based on a pair of angle and angle rate measurements. Variations on this cost function that included admissible regions and the error in projecting the state into future times were investigated as well.

The capabilities of these methods as tools for initial orbit determination were then assessed under a variety of scenarios. These included different observer and target orbital regimes for every combination of Low-Earth orbiting satellites and near-geosynchronous satellites. This was investigated both by generating contours for the cost function of single scenarios as well as Monte-Carlo tests to quantify the algorithms' capabilities for randomly generated scenarios of

Copyright © 2020 Advanced Maui Optical and Space Surveillance Technologies Conference (AMOS) – www.amostech.com

each type. It was shown that the Nelder-Mead optimizer improves over the particle swarm in both computation time and its ability to converge to the correct solution. Furthermore, it was shown that by adding the two cost functions together, the resulting cost function developed a favorable geometry for efficiently converging to the correct solution for near coplanar scenarios. Finally, the Nelder-Mead optimizer over the novel cost function was shown to be capable of converging to the correct solution for multi-orbit scenarios.

## 5. ACKNOWLEDGEMENTS

We thank Sue Hagerty for her assistance and advice on this research and report.

## REFERENCES

[1] Space track. `https://www.space-track.org/`, 5 2020.
[2] Stellarium. `http://stellarium.sourceforge.net/`, 5 2020. Version 0.16.1.
[3] Bruce A Conway. An improved algorithm due to laguerre for the solution of kepler's equation. *Celestial mechanics*, 39(2):199–211, 1986.
[4] Adam Danz. boxplotgroup. `https://www.mathworks.com/matlabcentral/fileexchange/74437-boxplotgroup`, MATLAB Central File Exchange, 2020. Retrieved May 21, 2020.
[5] Pedro Ramon Escobal. Methods of orbit determination. *New York: Wiley, 1965*, 1965.
[6] RH Gooding. A procedure for the solution of lambert's orbital boundary-value problem. *Celestial Mechanics and Dynamical Astronomy*, 48(2):145–165, 1990.
[7] Reza Raymond Karimi and Daniele Mortari. Initial orbit determination using multiple observations. *Celestial Mechanics and Dynamical Astronomy*, 109(2):167–180, 2011.
[8] Reza Raymond Karimi and Daniele Mortari. A performance based comparison of angle-only initial orbit determination methods. *Adv. Astronaut. Sci., AAS/AIAA, Hilton Head Island, South Carolina*, 150:1793–1809, 2013.
[9] Evan Kaufman, T Alan Lovell, and Taeyoung Lee. Nonlinear observability for relative orbit determination with angles-only measurements. *The Journal of the Astronautical Sciences*, 63(1):60–80, 2016.
[10] Jeffrey C Lagarias, James A Reeds, Margaret H Wright, and Paul E Wright. Convergence properties of the nelder–mead simplex method in low dimensions. *SIAM Journal on optimization*, 9(1):112–147, 1998.
[11] D. Lang, D. W. Hogg, K. Mierle, M. Blanton, and S. Roweis. Astrometry.net: Blind astrometric calibration of arbitrary astronomical images. *AJ*, 137:1782–2800, 2010. arXiv:0910.2233.
[12] Marco A Luersen and Rodolphe Le Riche. Globalized nelder–mead method for engineering optimization. *Computers & structures*, 82(23-26):2251–2260, 2004.
[13] John A Nelder and Roger Mead. A simplex method for function minimization. *The computer journal*, 7(4):308–313, 1965.
[14] John E Prussing and Bruce A Conway. *Orbital mechanics*. Oxford University Press, USA, 1993.
[15] Bob Schutz, Byron Tapley, and George H Born. *Statistical orbit determination*. Elsevier, 2004.
[16] Yuhui Shi and Russell C Eberhart. Parameter selection in particle swarm optimization. In *International conference on evolutionary programming*, pages 591–600. Springer, 1998.
[17] David A Vallado. *Fundamentals of astrodynamics and applications*, volume 12. Springer Science & Business Media, 2001.

*Copyright © 2020 Advanced Maui Optical and Space Surveillance Technologies Conference (AMOS) – www.amostech.com*